Journal of Power Sources 341 (2017) 318–326

Contents lists available at ScienceDirect

Journal of Power Sources

journal homepage: www.elsevier.com/locate/jpowsour

Highly catalytic and stabilized titanium nitride nanowire array-decorated graphite felt electrodes for all vanadium redox flow batteries

L. Wei [a], T.S. Zhao [a, *], L. Zeng [b], Y.K. Zeng [a], H.R. Jiang [a]

[a] Department of Mechanical and Aerospace Engineering, The Hong Kong University of Science and Technology, Clear Water Bay, Kowloon, Hong Kong, China
[b] HKUST Jockey Club Institute for Advanced Study, The Hong Kong University of Science and Technology, Clear Water Bay, Kowloon, Hong Kong SAR, China

HIGHLIGHTS

- Propose a binder-free TiN nanowire array-decorated electrode for VRFBs.
- Energy efficiency is up to 77.4% at 300 mA cm^{-2}, enhancing more than 15%.
- Electrolyte utilization is up to 73.9% at 300 mA cm^{-2}, enhancing more than 43%.
- High stability and capacity retention are achieved by present battery.

GRAPHICAL ABSTRACT

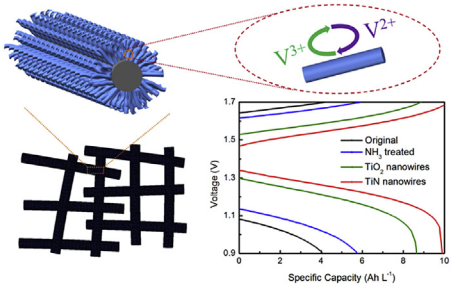

ARTICLE INFO

Article history:
Received 8 August 2016
Received in revised form
14 November 2016
Accepted 5 December 2016
Available online 10 December 2016

Keywords:
Vanadium redox flow battery
Redox chemistry
Electrode
Graphite felt
TiN nanowires

ABSTRACT

In this work, we prepare a highly catalytic and stabilized titanium nitride (TiN) nanowire array-decorated graphite felt electrode for all vanadium redox flow batteries (VRFBs). Free-standing TiN nanowires are synthesized by a two-step process, in which TiO_2 nanowires are first grown onto the surface of graphite felt via a seed-assisted hydrothermal method and then converted to TiN through nitridation reaction. When applied to VRFBs, the prepared electrode enables the electrolyte utilization and energy efficiency to be 73.9% and 77.4% at a high current density of 300 mA cm^{-2}, which are correspondingly 43.3% and 15.4% higher than that of battery assembled with a pristine electrode. More impressively, the present battery exhibits good stability and high capacity retention during the cycle test. The superior performance is ascribed to the significant improvement in the electrochemical kinetics and enlarged active sites toward V^{3+}/V^{2+} redox reaction.

1. Introduction

With increasingly pressing concerns over environmental issues and energy sustainability due to the consumption of fossil fuels, there has been a global agreement that renewable energies such as solar and wind are essential to economic and social development [1–3]. However, the fluctuant and intermittent nature of electricity generated from these renewables makes them less appealing for practical applications [4,5]. Underlying these considerations, the large-scale energy storage technology such as redox flow battery, offering well-established ability to improve grid reliability and utilization with inherent safety, moderate cost, ease of scalability and flexible operation, is an effective method to address this matter [6,7]. Particularly, the vanadium redox flow battery (VRFB) attracts the most attentions, owing to its advantages of significantly low

* Corresponding author.
E-mail address: metzhao@ust.hk (T.S. Zhao).

http://dx.doi.org/10.1016/j.jpowsour.2016.12.016
0378-7753/

cross-contamination and long service life by employing the same element, vanadium, in both positive and negative electrolytes [8,9].

VRFBs store and release electrical energy through electrochemical reactions of the VO_2^+/VO^{2+} and V^{3+}/V^{2+} redox species in the aqueous electrolyte. As a core component of the battery, the electrode provides electroactive surfaces and conducts electrons for redox reactions to take place [10]. Battery polarization, including the activation, ohmic and concentration losses are strongly dependent on the electrode and its surface chemistry [11]. In particular, the activation loss, which is plagued by the poor kinetic reversibility and electrochemical activity towards the vanadium redox reactions, has been a long-term barrier to improve the battery performance during the battery operation [12], often limiting the system to an operating current density lower than 100 mA cm^{-2} [13]. Thus, minimizing the polarization to endow the VRFBs with high energy efficiency at elevated operating current densities, best expressed as high power density, is always desired [14,15]. At the cell level, the augment of power density is effective for decreasing the size of the power stack, including the total area of bipolar plates, electrodes and membranes which represent a significant expense of the battery system [16].

Possessing wide operating potential range, satisfactory chemical and mechanical stability and availability with high electrical conductivity at low cost, carbonaceous materials such as graphite felts have been extensively used as electrodes in the past few decades [17]. Even though carbonaceous electrodes themselves already inherently possess catalytic effects towards vanadium species reactions, the optimization of electrode material is still a necessity to enhance the kinetics of the redox reactions [18]. To date, various surface modification approaches including the acid, thermal and nitrogen treatments have been introduced. While these techniques have been proved to create more active sites for vanadium redox reactions, excessive surface oxidation of carbon material leads to electrode corrosion and eventual disintegration [19]. An alternative approach to increase the active sites is to introduce nanostructured electrocatalysts on the surface of the electrode [20]. To date, a variety of metal-based (metal and metal oxide) and carbon-based materials (carbon nanotube, graphene, and carbon nanoparticles) with high electronic conductivities and specific surface areas have been reported in the literature [21–23]. The performance enhancement varies depending on the distribution uniformity and preparation process of the nanostructured electrocatalysts. High cost of noble metal catalysts as well as tedious synthesis procedures limited their practical application in VRFBs to some extent [24].

In recent years, transition metal carbides, nitrides and carbonitrides have been attracted increasing attention due to their remarkable properties such as high melting point, exceptional chemical stability, and high hardness [25]. Conductivity and catalytic activity of these types of catalysts are also comparable to those of metals [26]. In a recent publication, Wei et al. [27] and Yang et al. [28] performed pioneering work in applying TiC and TiN nanoparticles in aqueous media for catalyzing V^{3+}/V^{2+} redox reaction for VRFBs, respectively. These titanium carbide and nitride nanoparticles were employed to decorate on the surface of carbon fibers via binders to enhance the electrochemical activity of electrodes, enabling a high current-density operation.

In the present work, we propose the use of inexpensive and conductive TiN nanowires as catalysts to enhance the electrochemical activity of the graphite felt. Free-standing TiN nanowires were grown on the surface of graphite felt by a two-step process as illustrated in Fig. 1. TiO_2 nanowires were first grown onto the graphite felt via a seed-assisted hydrothermal method. The samples were subsequently thermally annealed in ammonia gas at a temperature above 700 °C, to convert them to TiN. When applied to flow batteries, the proposed electrode significantly improved the energy efficiency (the ratio of energy between the discharge and charge processes) of a VRFB by enhancing the kinetics of the sluggish V^{3+}/V^{2+} redox reaction, especially under high-power-density operation. In addition, it is demonstrated that the present battery exhibits a significantly improved rate capability and capacity retention during the cycle tests, in comparison to that of a pristine electrode. These superior results suggest that stabilized metal nitride nanomaterials could open up new avenues for the fabrication and application of high-performance electrodes for VRFBs. Fundamental understanding of the catalyst mechanism causing the improvement of battery performance was further discussed.

2. Experimental

2.1. Cyclic voltammetry and electrochemical impedance spectra

Cyclic voltammetry (CV) tests were obtained on a workstation (Autolab, PGSTAT30). A conventional three-electrode electrochemical cell was established with a glassy carbon electrode (GCE) with an area of 0.283 cm^2 as the working electrode, a saturated calomel electrode (SCE) as the reference electrode and a platinum mesh as the counter electrode. The GCE was modified by depositing different catalysts onto it and served as the working electrode as reported elsewhere [27]. 10 mg of commercialized TiN nanoparticles (Aldrich), Vulcan XC-72 carbon nanoparticles (E-TEK) with similar particle size were compared to identify the electrochemical activity of the TiN. These nanoparticles were separately dispersed to 1.9 mL ethanol, to which 0.1 mL of 5 wt% Nafion emulsion was added. After 50 min of sonication, a uniform suspension was achieved and 30 μL of the ink was pipetted on top of the GCE and dried in air. The measurement was performed at −0.7 V to 0 V (vs. SCE) in a solution containing 0.1 M VO^{2+} + 3 M H_2SO_4.

To further determine the rate determining step of the electrode reaction on the graphite felt electrode in this work, an electrochemical impedance spectra (EIS) test was performed with a potentiostat (EG&G Princeton, model 2273). A typical three-electrode system, in which the SGL graphite felt, a platinum mesh, and a saturated calomel electrode (SCE) were employed as the working electrode, counter electrode, and a reference electrode, respectively.

2.2. Fabrication of TiN nanowire decorated electrode

Binder-free TiN nanowires were directly grown on the surface of graphite felt via a two-step process. First, TiO_2 nanowires were grown on the graphite felt using a hydrothermal method as previously reported [29,30]: Graphite felt (SGL company, GFA series, 18 mm × 26 mm) was cleaned with ethanol and dried at 60 °C. Then, the graphite felt was immersed into a 0.2 M $TiCl_4$ aqueous solution (achieved by dissolving 1.10 mL $TiCl_4$ into 48.90 mL concentrated hydrochloric acid) for 30 min and dried in ambient air at room temperature for 10 h, forming the TiO_2 seeds on the surface of the graphite felt. 18.75 mL of concentrated hydrochloric acid, was added into 18.75 mL deionized water, and then mixed with 0.56 mL titanium n-butoxide. This solution, along with the TiO_2 seed coated graphite felt, was transferred to a Teflon-lined stainless autoclave (50 mL volume). The hydrothermal reaction was maintained at a constant temperature of 150 °C for 5.0 h in an electric oven and then cooled at room temperature. The sample was then sonicated with DI water for 5 min and dried at ambient air. This process uniformly covered the entire surface of the carbon fibers by a white film of TiO_2 nanowires. To convert TiO_2 to TiN, the samples were annealed in NH_3 at temperatures of 700, 800, and 900 °C for 1.5 h with a heating rate of 2 °C min^{-1}, respectively. The color of the

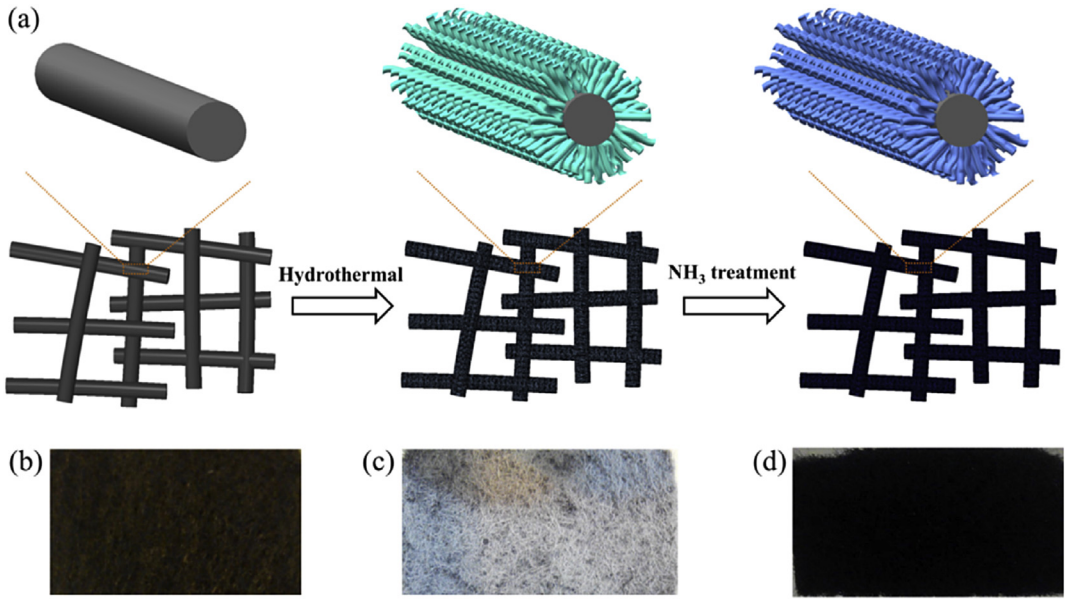

Fig. 1. (a) Schematic diagram of the two-step growth process for preparing TiN nanowires on the surface of graphite felt. Pictures of pristine graphite felt (b), graphite felt coated with TiO_2 nanowires (c), and TiN nanowires prepared in NH_3 atmosphere at 800 °C for 90 min (d).

nanowire film transformed from white to black subsequent to the annealing process, as depicted in Fig. 1d.

2.3. Material characterizations

The morphologies of the graphite felt electrodes were analyzed by scanning electron microscope (JEOL 6700F) at an acceleration voltage of 5.0 kV. Transmission electron-microscopy (TEM) images of TiN nanowires were measured by a high-resolution JEOL 2010F TEM system with a LaB_6 lament at 200 kV. The samples were dispersed in ethanol, sonicated and dripped onto regular carbon-coated Cu grids. The crystal phase and composition of the nanowires were analyzed by a Philips high-resolution X-ray diffraction system (XRD, model PW 1825) using a Cu-Ka source operating at 40 keV and a Micro-Raman spectrophotometer (Renishaw RM 3000) at an excitation wavelength of 514 nm. X-ray photoelectron spectroscopy (XPS) was performed using a Physical Electronics PHI 5600 multi-technique system equipped with an Al monochromatic X-ray source at a power of 350 W.

2.4. Flow battery performance test

Commercially available graphite felt (SGL company, GFA series) with an uncompressed thickness of 1.5 mm (active area of 4.7 cm^2) and prepared TiN nanowire array decorated graphite felt with the same size were used as positive and negative electrode, respectively. The pristine, NH_3 treated, and TiO_2 decorated graphite felts were also used as the negative electrodes for the purpose of comparison. 20 mL solution containing 1 M V^{3+} + 3 M H_2SO_4 and another 20 mL solution containing 1 M VO^{2+} + 3 M H_2SO_4 were employed as the negative and positive electrolytes. Nafion® NR-212 (Dupont) was applied as the membrane. The battery performance was tested in a zero-gap serpentine flow-field structured battery, which is detailed in our previous work [10], as illustrated in Fig. S1. The electrolytes in the batteries were circulated at a fixed flow rate of 0.6 mL s^{-1} with a peristaltic pump (N6-3L, Baoding Shenchen Precision Pump). Before each measurement, nitrogen gas (high purity) was bubbled to exhaust any entrapped air in the electrolyte and reservoirs. All measurements were conducted at room temperature. The performances of the VRFBs were assessed in a battery test system (BT2000, Arbin Instrument, Inc.).

The corresponding theoretical capacity and energy density of the battery in this work are 13.4 Ah L^{-1} and 18.8 Wh L^{-1}, respectively. The detailed calculation method is based on equation $C_{ap} = NC_aF/n$ and $E = NC_aFV/n$ reported by Li et al. [31], where C_{ap} is the capacity, E is the energy density, N is the number of electrons involved in the redox reaction, C_a is the concentration of the active redox species, F is the Faraday constant (26.8 Ah mol^{-1}), V is the voltage of the battery and n is the number of the electrolyte contributing to redox reactions.

3. Results and discussion

A typical transmission electron microscopy (TEM) image of commercialized TiN nanoparticles is shown in Fig. 2a; the average particle size of the TiN nanoparticles ranges from 30 to 50 nm, which is similar to that of the XC-72 carbon nanoparticles (average particle size: 40 nm) [10]. To identify the catalytic effect of TiN, CV measurements of commercialized TiN nanoparticles and XC-72 carbon nanoparticles toward V^{3+}/V^{2+} redox couple were compared and the results are shown in Fig. 2b. For the carbon nanoparticles electrode, poorly formed redox oxidation and reduction peaks are observed, indicating the catalytic activity of the electrode towards the V^{3+}/V^{2+} redox couple is rather low. It is also worth noting that the cathode current increases sharply as a result of the hydrogen evolution reaction at a more negative potential than −0.55 V (vs. SCE). The hydrogen evolution reaction appears to have a significant influence on the V^{3+} to V^{2+} reduction reaction on the carbon nanoparticles electrode [32]. As for the TiN electrode, a more pronounced redox peak appears as depicted from the CV curve. The anodic and cathodic peak currents for the redox reactions are considerably increased, and the peak potential separation is approximately 122 mV with a scan rate of 50 mV s^{-1}. This implies that the poor performance of the V^{3+}/V^{2+} couple is significantly enhanced by improving the electron transfer kinetics [33–35]. Furthermore, the onset potential of hydrogen evolution on the TiN electrode is significantly decreased compared with that on carbon nanoparticles, which implies that undesired side reaction in

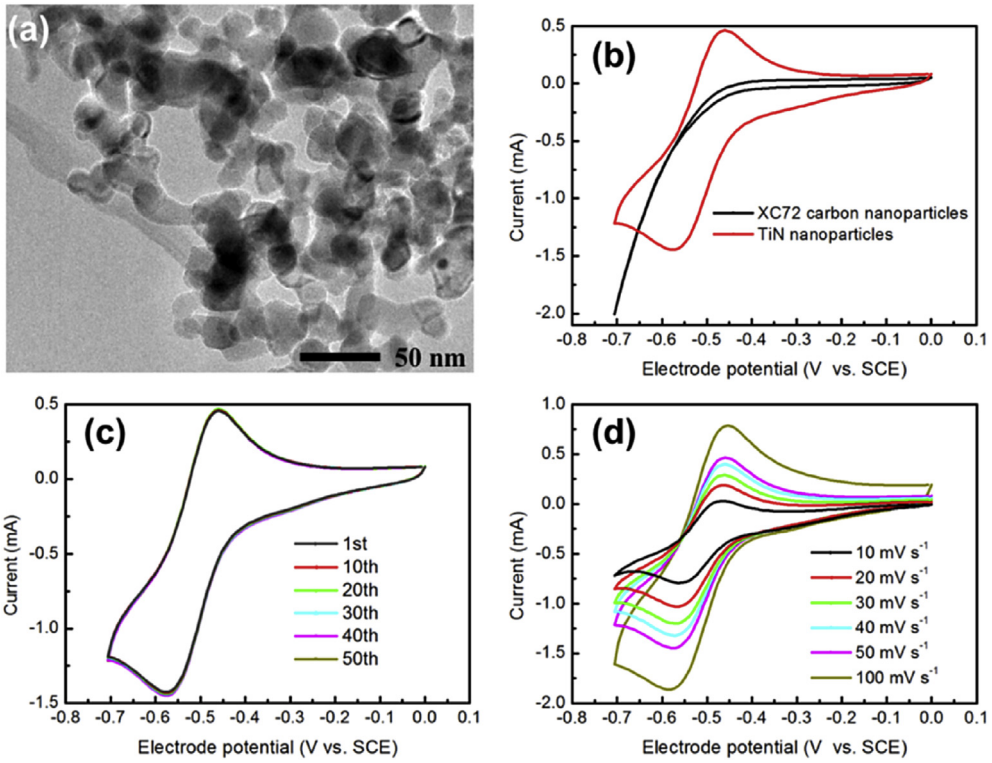

Fig. 2. (a) Typical TEM image of commercial TiN nanoparticles; (b) cyclic voltammograms for different electrode materials at a scan rate of 50 mV s^{-1} in a solution containing 0.1 M VO^{2+} and 3 M H_2SO_4; (c) repeating sweeping measurement of TiN nanoparticles at a scan rate of 50 mV s^{-1}; (d) cyclic voltammograms recorded on TiN nanoparticles at various scan rates.

VRFB systems, hydrogen evolution reaction, is also substantially suppressed [36]. Repetitive CVs were performed (50 scans at 50 mV s^{-1}, see Fig. 2c) to identify the durability of TiN as a catalyst for the redox reactions of the vanadium species. It is found that the curves exhibit good repeatability without significant degradation and the value of the anode peak current/cathode peak current remains essentially the same throughout the entire test process, which can be perceived as a first indication of the electrode stability. Fig. 2d displays the CV curves of TiN at different scan rates. The linear relationship ($R^2 = 0.993$ and $R^2 = 0.991$) between the anodic and cathodic peak currents and the square root of the scan rate observed on the TiN electrode indicates that the redox reaction is limited by its transport in the electrolyte in the range of scan rates [37].

The morphological structures of the TiN nanowires were performed by SEM characterization. Fig. 3a–c shows the representative morphology of the original graphite felt. From these figures it is seen that the carbon fibers are well-interconnected. The surface of the graphite felt is smooth without observable defects, providing an appropriate substrate for the growth of TiO_2 nanowires. The porous architecture of the electrode can facilitate the mass transport of the electrolyte during the charge/discharge processes [5,38]. After the hydrothermal reaction, a dense TiO_2 nanowire coverage was obtained due to well-dispersion of the precursor seeds (see Fig. 3d–f). These stabilized nanowires are directly linked to the surface of the graphite felt without any binder. A binder-free structure avoids the use of expensive Nafion suspensions, which not only helps to decrease the capital cost of the system [39], but also exposes the active surface of the electrode to the electrolytes to a larger extent since binders could potentially cover effective surface active sites for the redox reactions [40]. Further conversion of TiO_2 to TiN by annealing the samples in NH_3 at temperatures of 700, 800, and 900 °C was obtained and the results are shown in Fig. 3g–i, respectively. The morphology of the original TiO_2 nanowires is observed to be well-preserved at a temperature below 800 °C. However, when further heating at 900 °C, the original nanostructure was severely damaged. A majority of the nanowires collapsed and detached from the surface of graphite felt fibers. Therefore, increasing the heat treatment temperature benefits the nitridation reaction that converts TiO_2 to TiN [41], but leads to the destruction of the electrocatalysts nanostructures, which decreases the surface area and stability of the electrode. In this regard, an upper limit of the nitridation temperature at 800 °C is established in the following investigation.

To evaluate the physical properties of the obtained nanowires, XRD measurements were conducted to confirm the conversion of TiO_2 to TiN at different temperatures and the results are shown in Fig. 4a. The original TiO_2 sample shows several intense peaks of rutile TiO_2 (JCPDS: 21-1276). After the nitridation reaction occurred at a temperature above 700 °C, the obtained samples exhibit diffraction peaks at 36.7°, 42.6°, 61.8°, corresponding to the (111), (200) and (220) planes of the cubic TiN phase (JCPDS: 65-0714) [41]. Raman analyses are shown in Fig. 4b, it is found that the TiO_2 sample displays four characteristic peaks at around 145, 236, 445 and 609 cm^{-1}, which is attributed to the rutile TiO_2. After the nitridation reaction, it is observed that the Raman spectra is greatly changed and the TiN phase corresponding to the peaks at around 201, 323 and 552 cm^{-1} appear [29], indicating that the rutile TiO_2 could be completely converted to cubic TiN after annealing in NH_3 at a temperature of 800 °C, consistently with the results from XRD.

To further investigate the surface property of the samples, a contact angle measurement was performed by using the typical droplet method. As shown in Fig. S2, the wettability becomes significantly different in samples depending on the surface

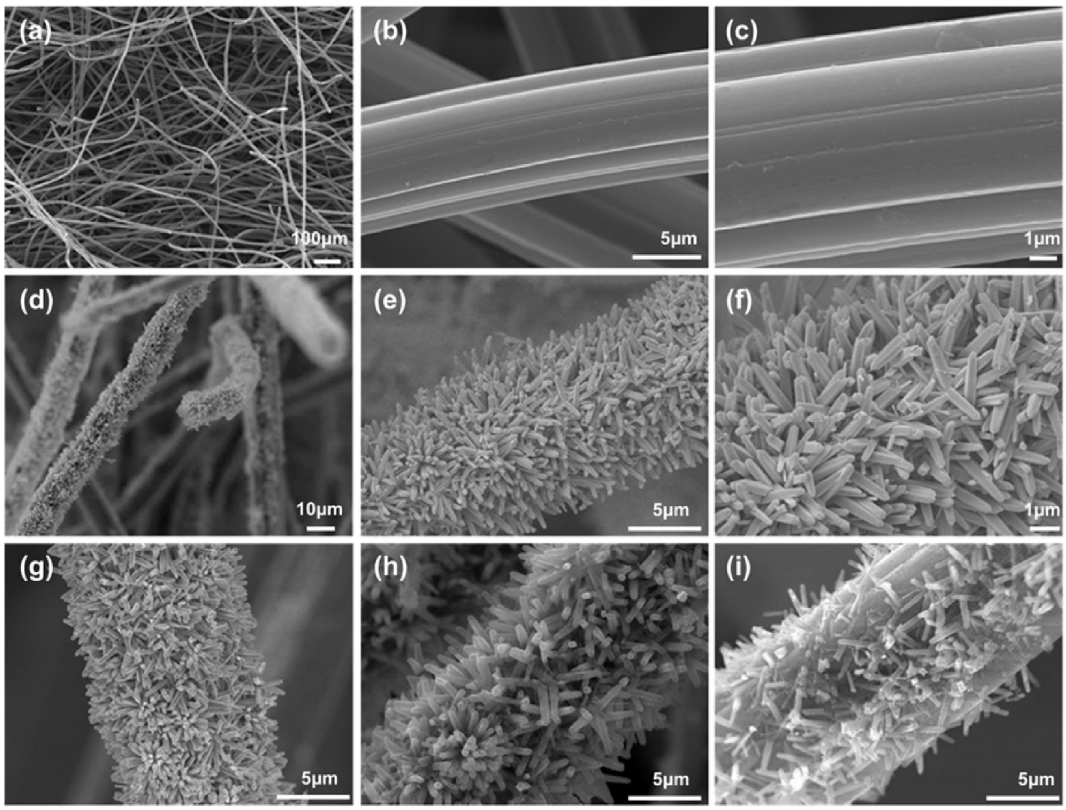

Fig. 3. SEM images collected for the original graphite felt (a–c); TiO_2 decorated electrode (d–f); and TiO_2 nanowires annealed in NH_3 at temperature of (g) 700 °C, (h) 800 °C, and (i) 900 °C.

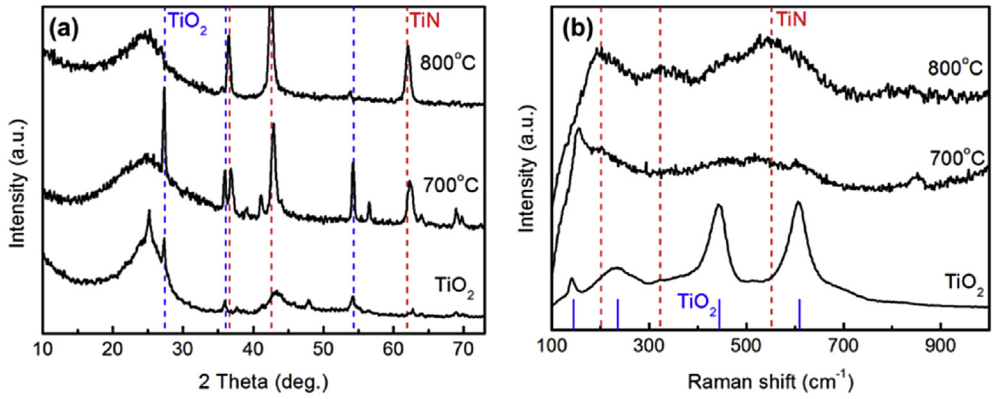

Fig. 4. XRD spectra (a) and Raman spectra (b) collected from TiO_2 and TiO_2 nanowires annealed in NH_3 at 700 and 800 °C. The blue and red dashed lines highlight peaks corresponding to rutile TiO_2 and cubic phase TiN, respectively. (For interpretation of the references to colour in this figure legend, the reader is referred to the web version of this article.)

modification process. Depending on the results, the measured contact angle is 120° for the pristine graphite felt. In contrast, it was difficult to measure the contact angle of TiO_2 and TiN (annealed at 800 °C) samples because it is immediately soaked when introduced to water, which indicates that the nature of electrode surface changes from hydrophobic to super hydrophilic through decoration of these nanowires. Eventually, improved electrolyte accessibility would be favorable for VRFB performance [42].

The crystal structure of the obtained TiN nanowires was analyzed further by high-resolution transmission electron microscopy (HRTEM). The sample was prepared by dropping nanowires onto the regular carbon film grid. As shown in Fig. S3, the diameters of the nanowires are in the range of 150–250 nm. Fig. 5a shows the HRTEM image of single typical nanowire. It can be seen from the figure that the exposed edges of TiN nanowire might act as active sites toward the redox reactions [36]. Fig. 5b displays the image of the crystal structure of the nanocrystals. The image reveals that the deposited nanowire possesses a high degree of crystallinity with an interfringe distance of about 0.2482 nm, which can be indexed to the (111) plane of the face-centered cubic-structured TiN. The high crystallinity can be also demonstrated from the fast Fourier transform (FFT) pattern, as presented inset of Fig. 5b.

To have an in-depth understanding of the surface chemical structures and oxidation state of the nanowires, energy dispersive

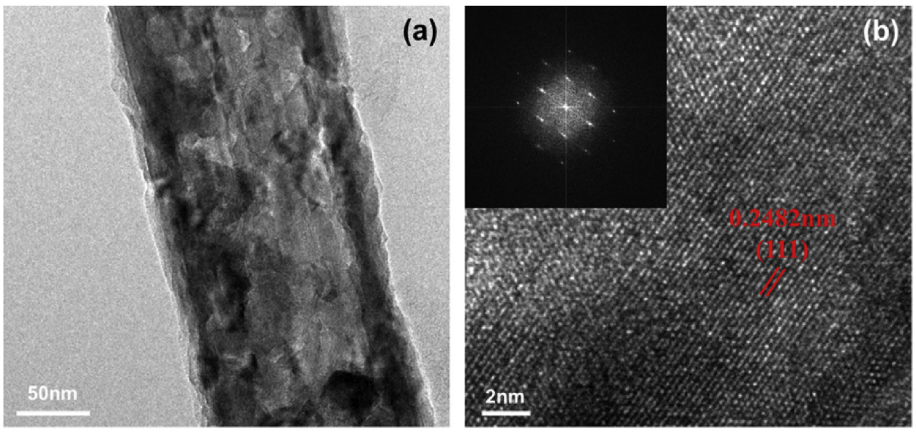

Fig. 5. (a) HRTEM image of one typical nanowire, (b) crystal structure of the TiN (nitrided at 800 °C) nanocrystals and corresponding fast Fourier transform (FFT) pattern.

X-ray spectroscopy (EDS) and XPS characterizations were determined and the results are shown in Fig. S4 and Fig. 6. EDS elemental mapping results show that the elements are uniformly distributed in the nanowire. A trace amount of oxygen detected suggests the presence of TiO_2 or TiO_xN_y in the TiN nanowires. XPS spectra of the TiN nanowires confirm the presence of N, while no N signal is found for the pristine TiO_2 samples, as expected. The Ti 2p spectrum of the pristine TiO_2 exhibits the binding energy of 459.3 eV ascribed to the Ti 2p3/2 of TiO_2 nanowires [30]. It is noteworthy to mention that, after nitridation, multiple peaks are deconvoluted at lower binding energies, which can be assigned to be Ti–N ($2p_{3/2}$ = 455.6–455.9 eV and $2p_{1/2}$ = 461.4–461.8 eV), Ti–N–O ($2p_{3/2}$ = 457.1–457.5 eV and $2p_{1/2}$ = 463.1–463.5 eV), and Ti–O ($2p_{3/2}$ = 458.7–459.3 eV and $2p_{1/2}$ = 464.4–465.0 eV) [43]. The residual Ti–O bond on the surface is mainly attributed to the inefficient nitridation and partial oxidation in the ambient air [44]. The fact that new Ti–N–O and Ti–N peaks appeared during nitradation indicates that the surface of NH_3-treated TiO_2 nanowire is composed of Ti–N–O, Ti–N, and Ti–O chemical states [29].

To demonstrate the practical application of the proposed electrode in the VRFB, the electrochemical properties of the TiN nanowires decorated graphite felt were further studied by typical charge–discharge measurements. Fig. 7a shows the voltage profiles of batteries at the same current density of 300 mA cm^{-2}. The original graphite felt, NH_3-treated and TiO_2 nanowires decorated electrode are employed as references, respectively. Under the fixed voltage region between 0.9 and 1.7 V, the cell employing pristine graphite felt exhibits poor discharge capacity (4.1 Ah L^{-1}, 30.6% of theoretical capacity), indicating that battery performance is low due to severe polarization. This is mainly caused by an insufficient number of surface active sites for the vanadium redox reactions on the electrode. In comparison to the pristine electrode, the NH_3 treated one displays a slightly reduced overpotential and increased capacity (5.7 Ah L^{-1}, 42.5% of theoretical capacity) in both charge and discharge processes owing to the presence of nitrogen functional groups. However, it is worth mentioning that an excess of these kind of surface functional groups could reduce the electron conductivity of the electrode, thus leading to increased ohmic loss during high current density operation [19]. For the electrode decorated with TiO_2 nanowires (8.6 Ah L^{-1}, 64.2% of theoretical capacity), the overpotentials further decreased in the corresponding charge and discharge processes due to improved hydrophilicity and an enlarged electrochemical surface area. More impressively, the cell installed with the TiN nanowires electrode exhibits the largest capacity (9.9 Ah L^{-1}, 73.9% of theoretical capacity), lowest charge voltage plateau, and highest discharge voltage plateau. This indicates that the TiN decorated electrode shows superior electrochemical properties compared with the original, N-doped and TiO_2 decorated electrodes. The superior electrochemical performance can be attributed to the surface properties of the TiN nanowires. Specifically, the conductive and hydrophilic layer of the TiN, as well as its high surface area with abundant active sites, greatly accelerates the redox reaction, especially at high charge/discharge rates, presumably by lowering the kinetic activation energy for the redox reaction [12]. The improvement in the specific capacity, which is identified as increased utilization of the electrolyte [45,46], will contribute efficiently to capital cost reduction as vanadium salts account for nearly 40% of the system cost [47].

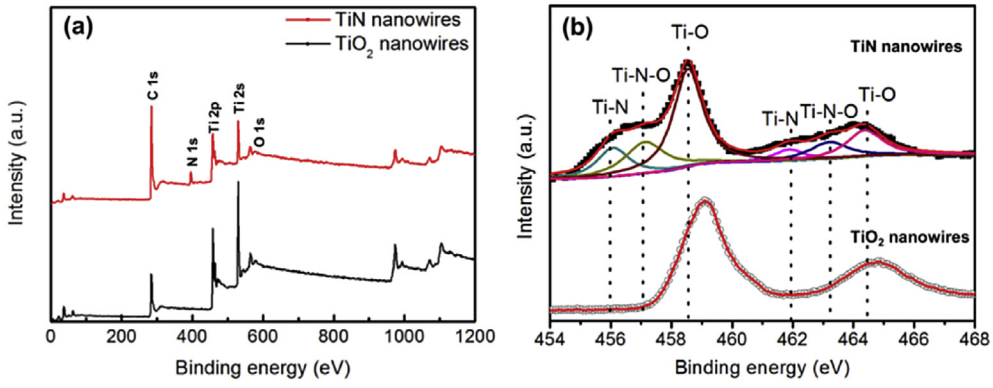

Fig. 6. XPS survey (a) and Ti 2p XPS spectra (b) of the TiO_2 and TiN nanowire (nitrided at 800 °C) decorated electrode.

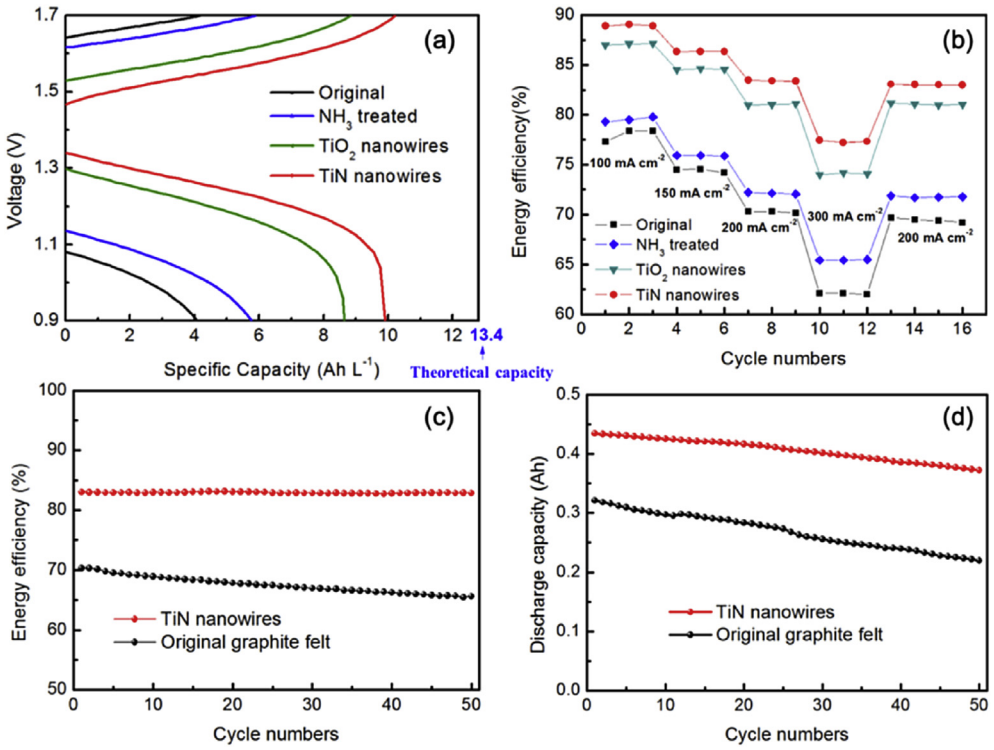

Fig. 7. Electrochemical performance of VRFBs quipped with pristine, NH_3 treated, TiO_2 decorated and TiN nanowire (nitrided at 800 °C) array-decorated graphite felt electrodes. (a) Charge and discharge curve at 300 mA cm^{-2}; (b) energy efficiency as a function of cycle number at different current densities. Cycling tests of VRFBs with and without TiN nanowire decorated electrode: (c) energy efficiency and (d) discharge capacity of VRFBs at a current density of 200 mA cm^{-2}.

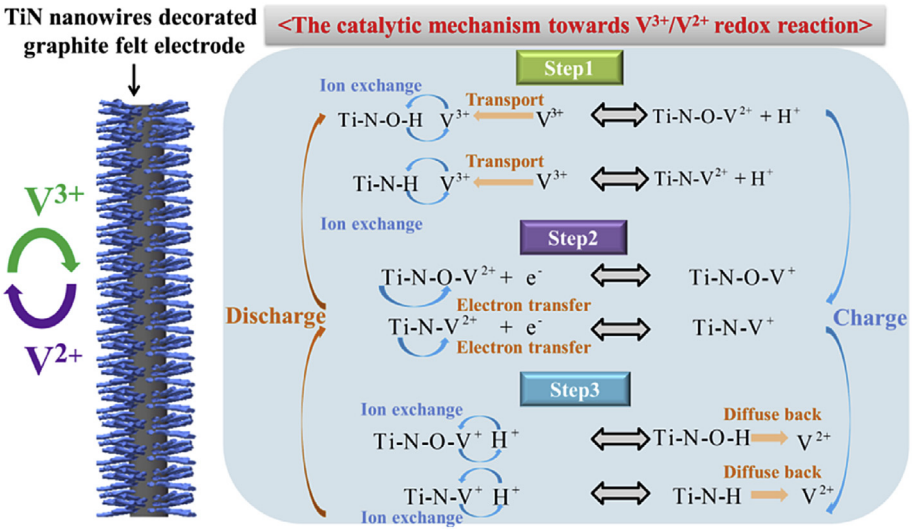

Fig. 8. Schematic illustration of the mechanism for the V^{3+}/V^{2+} redox reaction occurring in the presence of TiN nanowires on the surface of graphite felt electrode.

Additionally, the rate capability test of the samples was performed as increasing current densities from 100 to 300 mA cm^{-2} (see Fig. 7b). After being decorated with TiN nanowire arrays, the battery exhibits a substantially improved rate capability, as expected. Even at a current density as high as 300 mA cm^{-2}, the energy efficiency reaches 77.4%, which is 15.4%, 12% and 3.5% higher than that of the battery with pristine, NH_3 treated and TiO_2 nanowires decorated graphite felt electrode, respectively. Notably, to assess the stability of the TiN decorated electrode, the operating current from 300 to 200 mA cm^{-2} at the thirteenth cycle is swiftly changed and noted that the battery performance was fully recovered, indicating that the chemical and electrochemical robustness of the TiN decorated electrode in negative electrolyte [11].

A VRFB's stability is of critical importance for practical applications [47]. To further identify the stability and suitability of the proposed electrode during battery operation, cycling tests of VRFBs with and without TiN decorated electrodes were conducted at a current density of 200 mA cm^{-2}. As depicted in Fig. 7c, the energy efficiency of the battery with the proposed electrode sustained an enhanced initial improvement of 13% compared to that of the

pristine battery and the value stayed at above 82.8% without observable decay. Fig. 7d displays corresponding discharge capacities within cycles. The capacity of the present battery maintained above 86% of the initial value after 50 cycles, displaying an average capacity decay rate of merely 0.28% per cycle, equaling to apparently higher capacity retention compared to that of the pristine electrode. These results further demonstrate the excellent stability of the electrocatalytic effect brought by TiN nanowires over repeated cycling. On the basis of the experimental results, the TiN nanowires decorated electrode was proved to be an effective electrode in the VRFB system primarily due to their high catalytic activity towards the V^{3+}/V^{2+} redox reaction. According to our EIS test results (see Fig. S5), the charge transfer resistance of V^{3+}/V^{2+} and VO_2^+/VO^{2+} redox on the graphite felt is 14.96 and 0.91 Ω cm^2, respectively. The VO_2^+/VO^{2+} redox couple shows much more facile kinetics than the V^{3+}/V^{2+} couple, which indicates that catalysis efforts should be focused on V^{3+}/V^{2+} in the negative side rather than the VO_2^+/VO^{2+} in the positive side (in consistence with the kinetic studies of vanadium redox couples reported by Prof. Mench [48,49] and Shao-Horn group [50]).

Through clear confirmation of the performance improvement by introducing TiN nanowires, a possible explanation for the catalytic mechanism for the vanadium redox reaction can be speculated guided by the early study of Skyllas-Kazacos et al. [51,52], as shown in Fig. 8. Taking the charge process as an example; the first step in the reaction involves an ion exchange process between V^{3+} ions transported from the bulk of the electrolyte and the hydrogen ions of the Ti—N—O—H and Ti—N—H. Thus, V^{3+} ions can be absorbed with ease on the Ti—N and Ti—N—O functional layer. In the second step, electron transfer, facilitated by Ti—N and Ti—N—O bonds acting as an electron donor, takes place from V^{3+} to V^{2+} along the bonds. In the final step, the reduction reaction is terminated by an ion-exchange between the V^{2+} formed on the electrode surface and the hydrogen ions in the electrolyte. During the discharge process, a similar oxidation reaction in the opposite direction occurs. It is worth mentioning that the pristine TiO_2 has a large band-gap and low electrical conductivity, but the band-gap deceases and electrical conductivity enhances after the N-doping process [53,54]. Yang et al. [55] investigated the effect of N concentrations on the electrical conductivity of TiO_2. They found that as the N concentration increased from 0 to 1.39%, and then to 4.17%, TiO_2 gradually transformed to metallic states. The increasing electrical conductivity from TiO_2 to TiN provides an explanation for the better battery performance of TiN than TiO_2 decorated electrode.

4. Conclusion

In summary, using a two-step approach, we synthesized a highly catalytic and binder-free TiN nanowire array decorated graphite felt electrode for VRFBs. Substantial enhancement in battery performance, including energy efficiency and utilization of the electrolyte, is attributed to the outstanding catalytic effect of decorated TiN nanowires on the surface of the electrode. Even at a current density of as high as 300 mA cm^{-2}, the energy efficiency reached 77.4%, and the utilization of electrolyte reached 73.9% of the theoretical capacity, which is among the highest performance of VRFBs recorded in the literature. Moreover, the battery equipped with the proposed electrode was demonstrated to show excellent stability and high capacity retention during the cycling test. It is believed that this work offers a new approach for fabricating high-performance electrode, and contributes to the development of transition metal nitrides nanomaterials in VRFB technology to achieve a superior battery performance.

Acknowledgements

The work described in this paper was fully supported by a grant from the Research Grants Council of the Hong Kong Special Administrative Region, China (Project No. 623313).

Appendix A. Supplementary data

Supplementary data related to this article can be found at http://dx.doi.org/10.1016/j.jpowsour.2016.12.016.

References

[1] Q. Xu, T.S. Zhao, Prog. Energy Combust. Sci. 49 (2015) 40–58.
[2] P.K. Leung, X. Li, C. Ponce de León, L. Berlouis, C.T.J. Low, F.C. Walsh, RSC Adv. 2 (2012) 10125.
[3] C. Ding, H.M. Zhang, X.F. Li, T. Liu, F. Xing, J. Phys. Chem. Lett. 4 (2013) 1281–1294.
[4] R.M. Darling, K.G. Gallagher, J.A. Kowalski, S. Ha, F.R. Brushett, Energy & Environ. Sci. 7 (2014) 3459–3477.
[5] P. Leung, M. Mohamed, A. Shah, Q. Xu, M. Conde-Duran, J. Power Sources 274 (2015) 651–658.
[6] J. Noack, N. Roznyatovskaya, T. Herr, P. Fischer, Angew. Chem. Int. Ed. 54 (2015) 9776–9809.
[7] K. Lin, Q. Chen, M.R. Gerhardt, L. Tong, S.B. Kim, L. Eisenach, A.W. Valle, D. Hardee, R.G. Gordon, M.J. Aziz, Science 349 (2015) 1529–1532.
[8] M. Skyllas-Kazacos, M.H. Chakrabarti, S.A. Hajimolana, F.S. Mjalli, M. Saleem, J. Electrochem. Soc. 158 (2011) R55.
[9] X.L. Zhou, T.S. Zhao, L. An, L. Wei, C. Zhang, Electrochim. Acta 153 (2015) 492–498.
[10] L. Wei, T. Zhao, G. Zhao, L. An, L. Zeng, Appl. Energy 176 (2016) 74–79.
[11] P.K. Leung, J. Palma, E. Garcia-Quismondo, L. Sanz, M. Mohamed, M. Anderson, J. Power Sources 310 (2016) 1–11.
[12] K.J. Kim, H.S. Lee, J. Kim, M.S. Park, J.H. Kim, Y.J. Kim, M. Skyllas-Kazacos, ChemSusChem 9 (2016) 1329–1338.
[13] B. Sun, M. Skyllas-Kazacos, Electrochim. Acta 37 (1992) 2459–2465.
[14] X.L. Zhou, Y.K. Zeng, X. Zhu, L. Wei, T.S. Zhao, J. Power Sources 325 (2016) 329–336.
[15] Y. Zeng, X.L. Zhou, L. An, L. Wei, T.S. Zhao, J. Power Sources 324 (2016) 738–744.
[16] D.S. Aaron, Q. Liu, Z. Tang, G.M. Grim, A.B. Papandrew, A. Turhan, T.A. Zawodzinski, M.M. Mench, J. Power Sources 206 (2012) 450–453.
[17] K.J. Kim, Y.-J. Kim, J.-H. Kim, M.-S. Park, Mater. Chem. Phys. 131 (2011) 547–553.
[18] A. Parasuraman, T.M. Lim, C. Menictas, M. Skyllas-Kazacos, Electrochim. Acta 101 (2013) 27–40.
[19] A. Di Blasi, O. Di Blasi, N. Briguglio, A.S. Aricò, D. Sebastián, M.J. Lázaro, G. Monforte, V. Antonucci, J. Power Sources 227 (2013) 15–23.
[20] M. Park, J. Ryu, J. Cho, Chem. Asian J. 10 (2015) 110.
[21] Z. Gonzalez, S. Vizireanu, G. Dinescu, C. Blanco, R. Santamaria, Nano Energy 1 (2012) 833–839.
[22] M. Ulaganathan, A. Jain, V. Aravindan, S. Jayaraman, W.C. Ling, T.M. Lim, M.P. Srinivasan, Q. Yan, S. Madhavi, J. Power Sources 274 (2015) 846–850.
[23] P. Han, Y. Yue, Z. Liu, W. Xu, L. Zhang, H. Xu, S. Dong, G. Cui, Energy & Environ. Sci. 4 (2011) 4710.
[24] B. Li, M. Gu, Z. Nie, Y. Shao, Q. Luo, X. Wei, X. Li, J. Xiao, C. Wang, V. Sprenkle, W. Wang, Nano Lett. 13 (2013) 1330–1335.
[25] S.T. Oyama, Catal. Today 15 (1992) 179–200.
[26] H.H. Hwu, J.G.G. Chen, Chem. Rev. 105 (2005) 185–212.
[27] L. Wei, T.S. Zhao, L. Zeng, X.L. Zhou, Y.K. Zeng, Energy Technol. Ger. 4 (2016) 990.
[28] C.M. Yang, H.N. Wang, S.F. Lu, C.X. Wu, Y.Y. Liu, Q.L. Tan, D.W. Liang, Y. Xiang, Electrochim. Acta 182 (2015) 834–840.
[29] X.H. Lu, G.M. Wang, T. Zhai, M.H. Yu, S.L. Xie, Y.C. Ling, C.L. Liang, Y.X. Tong, Y. Li, Nano Lett. 12 (2012) 5376–5381.
[30] G.M. Wang, H.Y. Wang, Y.C. Ling, Y.C. Tang, X.Y. Yang, R.C. Fitzmorris, C.C. Wang, J.Z. Zhang, Y. Li, Nano Lett. 11 (2011) 3026–3033.
[31] B. Li, Z.M. Nie, M. Vijayakumar, G.S. Li, J. Liu, V. Sprenkle, W. Wang, Nat. Commun. 6 (2015).
[32] P.K. Leung, C. Ponce-de-León, C.T.J. Low, A.A. Shah, F.C. Walsh, J. Power Sources 196 (2011) 5174–5185.
[33] L. Shi, S.Q. Liu, Z. He, J.X. Shen, Electrochim. Acta 138 (2014) 93–100.
[34] M. Park, J. Ryu, Y. Kim, J. Cho, Energy & Environ. Sci. 7 (2014) 3727–3735.
[35] M. Park, I.Y. Jeon, J. Ryu, J.B. Baek, J. Cho, Adv. Energy Mater 5 (2015).
[36] M. Park, Y.J. Jung, J. Kim, H. Lee, J. Cho, Nano Lett. 13 (2013) 4833–4839.
[37] J.H. Kim, K.J. Kim, M.S. Park, N.J. Lee, U. Hwang, H. Kim, Y.J. Kim, Electrochem. Commun. 13 (2011) 997–1000.
[38] S.Y. Wang, X.S. Zhao, T. Cochell, A. Manthiram, J. Phys. Chem. Lett. 3 (2012) 2164–2167.
[39] M.L. Perry, A.Z. Weber, J. Electrochem. Soc. 163 (2016) A5064–A5067.
[40] G. Sasikumar, J.W. Ihm, H. Ryu, Electrochim. Acta 50 (2004) 601–605.

[41] Y. Ren, Z. Ren, J. Li, S. Wang, J. Yu, RSC Adv. 5 (2015) 106439–106443.
[42] H. Zhou, J. Xi, Z. Li, Z. Zhang, L. Yu, L. Liu, X. Qiu, L. Chen, RSC Adv. 4 (2014) 61912–61918.
[43] I. Milosev, H.H. Strehblow, B. Navinsek, M. Metikoshukovic, Surf. Interface Anal. 23 (1995) 529–539.
[44] Y.J. Wei, C.W. Peng, T.M. Cheng, H.K. Lin, Y.L. Chen, C.Y. Lee, H.T. Chiu, Acs Appl. Mater Inter 3 (2011) 3804–3812.
[45] Q. Zheng, F. Xing, X.F. Li, T. Liu, Q.Z. Lai, G.L. Ning, H.M. Zhang, J. Power Sources 266 (2014) 145–149.
[46] A. Di Blasi, N. Briguglio, O. Di Blasi, V. Antonucci, Appl. Energy 125 (2014) 114–122.
[47] Y. Zeng, T. Zhao, L. An, X. Zhou, L. Wei, J. Power Sources 300 (2015) 438–443.
[48] D. Aaron, C.N. Sun, M. Bright, A.B. Papandrew, M.M. Mench, T.A. Zawodzinski, Ecs Electrochem Lett. 2 (2013) A29–A31.
[49] C.N. Sun, F.M. Delnick, D.S. Aaron, A.B. Papandrew, M.M. Mench, T.A. Zawodzinski, Ecs Electrochem Lett. 2 (2013) A43–A45.
[50] N. Pour, D.G. Kwabi, T. Carney, R.M. Darling, M.L. Perry, Y. Shao-Horn, J. Phys. Chem. C 119 (2015) 5311–5318.
[51] K.J. Kim, M.S. Park, Y.J. Kim, J.H. Kim, S.X. Dou, M. Skyllas-Kazacos, J. Mater Chem. A 3 (2015) 16913–16933.
[52] S. Zhong, M. Skyllas-Kazacos, J. Power Sources 39 (1992) 1–9.
[53] A. Nambu, J. Graciani, J. Rodriguez, Q. Wu, E. Fujita, J.F. Sanz, J. Chem. Phys. 125 (2006) 094706.
[54] C. Di Valentin, E. Finazzi, G. Pacchioni, A. Selloni, S. Livraghi, M.C. Paganini, E. Giamello, Chem. Phys. 339 (2007) 44–56.
[55] K. Yang, Y. Dai, B. Huang, J. Phys. Chem. C 111 (2007) 12086–12090.